Title
Integration of High-Resolution Radiation Detector for Hybrid Microchip Electrophoresis

Journal
Analytical Chemistry, 92(4)

ISSN
0003-2700

Authors
Jones, Jason
Ha, Noel S
Barajas, Alec G
et al.

Publication Date
2020-02-18

DOI
10.1021/acs.analchem.9b04827

Peer reviewed

analytical chemistry

pubs.acs.org/ac Article

Integration of High-Resolution Radiation Detector for Hybrid Microchip Electrophoresis

Jason Jones, Noel S. Ha, Alec G. Barajas, Arion F. Chatziioannou, and R. Michael van Dam*

Cite This: *Anal. Chem.* 2020, 92, 3483−3491 Read Online

ABSTRACT: For decades, there has been immense progress in miniaturizing analytical methods based on electrophoresis to improve sensitivity and to reduce sample volumes, separation times, and/or equipment cost and space requirements, in applications ranging from analysis of biological samples to environmental analysis to forensics. In the field of radiochemistry, where radiation-shielded laboratory space is limited, there has been great interest in harnessing the compactness, high efficiency, and speed of microfluidics to synthesize short-lived radiolabeled compounds. We recently proposed that analysis of these compounds could also benefit from miniaturization and have been investigating capillary electrophoresis (CE) and hybrid microchip electrophoresis (hybrid-MCE) as alternatives to the typically used high-performance liquid chromatography (HPLC). We previously showed separation of the positron-emission tomography (PET) imaging tracer 3′-deoxy-3′-fluorothymidine (FLT) from its impurities in a hybrid-MCE device with UV detection, with similar separation performance to HPLC, but with improved speed and lower sample volumes. In this paper, we have developed an integrated radiation detector to enable measurement of the emitted radiation from radiolabeled compounds. Though conventional radiation detectors have been incorporated into CE systems in the past, these approaches cannot be readily integrated into a compact hybrid-MCE device. We instead employed a solid-state avalanche photodiode (APD)-based detector for real-time, high-sensitivity β particle detection. The integrated system can reliably separate [^{18}F]FLT from its impurities and perform chemical identification via coinjection with nonradioactive reference standard. This system can quantitate samples with radioactivity concentrations as low as 114 MBq/mL (3.1 mCi/mL), which is sufficient for analysis of radiochemical purity of radiopharmaceuticals.

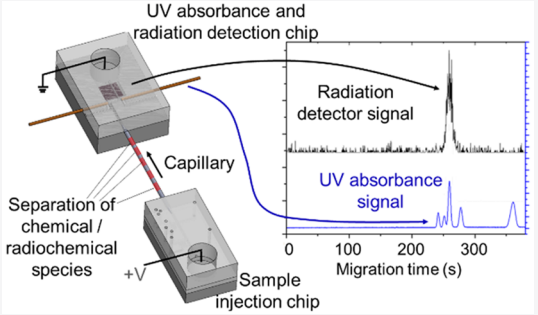

Capillary electrophoresis (CE) has been used in a wide variety of fields such as separation of biomolecules,[1−3] environmental monitoring,[4,5] food analysis,[6,7] and forensics.[8] Typically, compounds are detected via UV absorbance,[9] though many additional modes of detection can be implemented, including pulsed amperometric detection,[10] capacitively coupled contactless conductivity detection,[11−13] refractive index detection,[14] mass spectrometry,[15,16] and fluorescence.[17,18] CE has also been used for separation of radioactive compounds in applications such as assessing the purity of radiopharmaceuticals labeled with positron-emitting isotopes for positron-emission tomography (PET) or with gamma-emitting isotopes for single photon emission computed tomography (SPECT),[19,20] as well as the analysis of radioisotopes in nuclear fuel development.[21,22]

Due to the small sample volumes used in CE, detectors and flow cells must be designed to maximize detection efficiency, especially for radiation detection. Several radiation detection approaches have been reported in the literature for CE applications. For example, Altria et al. placed a NaI(TI) crystal scintillator and photomultiplier tube (PMT) adjacent to a capillary for detection of γ rays from [^{99m}Tc]TcO_4- and various chelates.[23] Due to the long-range of γ rays, a lead collimator was used to localize the detection volume. Jankowsky et al. threaded the capillary through an NaI crystal for detecting various ^{99}Tc-labeled compounds and reported a detection efficiency of 85.4%.[20,24] Klunder et al. passed the capillary through a plastic scintillator with an added reflective coating to increase light collection and achieved detection efficiencies for beta particles emitted from the lanthanide fission products Eu-152 and Cs-137 of ∼60% and ∼80%, respectively.[25] In a report by Kaniansky et al., the flow cell was a small channel through a thin layer of a plastic scintillator sandwiched between layers of transparent plastic and dual PMTs. The thin geometry was designed to shrink the detection region to improve resolution but came at the expense of a lower detection efficiency—only 13−15% for ^{14}C-labeled compounds.[26] Pentoney et al. reported an alternative way to improve detection sensitivity via "flow programming", in which the separation voltage was reduced when a "band" (corresponding to a particular

Received: October 22, 2019
Accepted: January 28, 2020
Published: January 28, 2020

https://dx.doi.org/10.1021/acs.analchem.9b04827
Anal. Chem. 2020, 92, 3483−3491

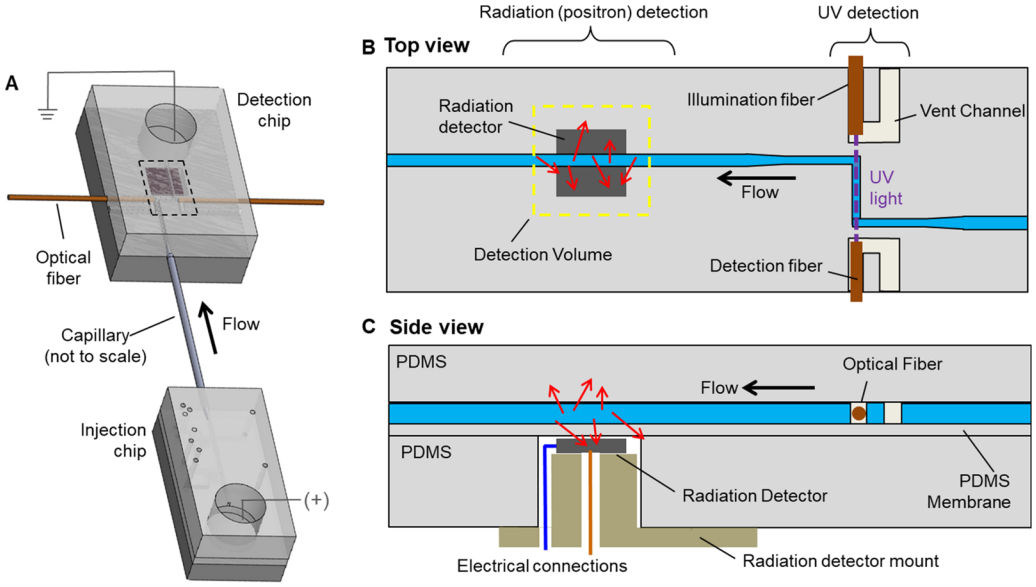

Figure 1. (A) 3D rendering of the hybrid-MCE device design, comprising an injection chip, capillary, and detection chip. (B) Top view schematic (not to scale) of detection chip showing both the UV absorbance and radiation detection regions. Red arrows represent positron emissions from the sample. The sensitive region of the radiation detector extends ~1 mm beyond the edges of the detector for positrons from F-18. (C) Side view schematic (not to scale) of the detection chip.

radioactive species) was in the detection region, to increase the residence time.[19,27] Using a detection geometry where the capillary passed through a 2 mm thick plastic scintillator with reflective coating adjacent the PMT, mixtures of ^{32}P-labeled molecules were detected with 65% efficiency.

Despite these examples of successful analysis via CE, analysis of radiochemicals is nearly always performed with radio-high-performance liquid chromatography (radio-HPLC). We have been exploring the analysis of radiopharmaceuticals with CE as an alternative to HPLC[28] due to the potential advantages of smaller sample volume and faster separation time (important for short-lived compounds), the potential for miniaturization into extremely compact microchip electrophoresis (MCE) devices,[29,30] and less need for shielding. A MCE setup is expected to have similar separating power as HPLC but significantly lower cost and smaller footprint—important in radiochemistry applications where radiation-shielded laboratory space is at a premium. Importantly, MCE also has the benefit of high flexibility of flow cell geometry and detector integration that can be implemented into a microfluidic format. Ultimately this approach could reduce the resources needed for radiopharmaceutical analysis and could become an integral part of emerging, compact microfluidic radiopharmaceutical production systems.[31,32] We previously demonstrated the analysis of the nonradioactive form of the PET tracer 3′-deoxy-3′-[^{18}F]fluorothymidine ([^{18}F]FLT) and its known impurities using a conventional CE system,[28] as well as a hybrid-MCE system that we developed,[33,34] both using UV absorbance detection, and found the separation efficiency and UV sensitivity to be similar to HPLC.

To our knowledge, radiation detection has not been reported in conjunction with MCE. The key challenges are to maximize (i) sensitivity (due to the very small injection volume and thus low amount of radioactivity and the very short time in which the sample is in the field of view of the detector) and (ii) spatial localization (to ensure that the detector is only sensitive to radiation from a dedicated small section of the chip at the exit of the separation channel). Using analysis of radiolabeled imaging tracers as an example application,[35−37] the expected radioactivity concentrations of the samples could range from ~37 MBq/mL (a dilute batch sufficient for imaging a single patient) to ~10 GBq/mL (a large multipatient batch produced in a radiopharmacy for distribution to multiple imaging sites). Since MCE uses sample volumes in the nL range, high sensitivity is of paramount importance.

The aforementioned radiation detection techniques for CE cannot be easily integrated into MCE setups due to the bulky nature of PMTs, the need to route the capillary through the scintillating material itself, or the need for extensive shielding and collimation. However, numerous groups have integrated more compact radiation detectors into microfluidic devices for a variety of applications,[31] which can potentially be applied to MCE. An advantage of working with beta+ or positron-emitting compounds is that the positron range is relatively small (e.g., <1 mm for fluorine-18 in water) and thus shielding can be largely avoided provided the detector has much higher sensitivity to positrons than γ rays (resulting from annihilation of positrons). This could be achieved using a thin, low-Z scintillator coupled to a sensitive photodetector[38] or a thin solid-state detector.[39] Of course due to this short particle range, it is critical that the detector or scintillator be located very close to the radioactive source.[40]

Cho et al. used a CCD camera to observe the distribution of ^{18}F-labeled compounds within a microfluidic chip mounted adjacent a thin scintillator layer. Though the scintillator had large lateral dimensions, by monitoring only a small subset of pixels, sensitive detection in a localized area was possible (185 Bq in 1 mm^2).[41] Using a silicon photomultipler (SiPM) in place of a PMT or CCD camera allows for a large reduction in instrument size while maintaining high sensitivity. Tarn et al. used an SiPM array adjacent a thin plastic scintillator containing a machined 0.7 μL flow cell,[42] in which each SiPM element monitored a localized region of the chip. Interestingly, SiPM pixels have also been used to directly

https://dx.doi.org/10.1021/acs.analchem.9b04827
Anal. Chem. 2020, 92, 3483−3491

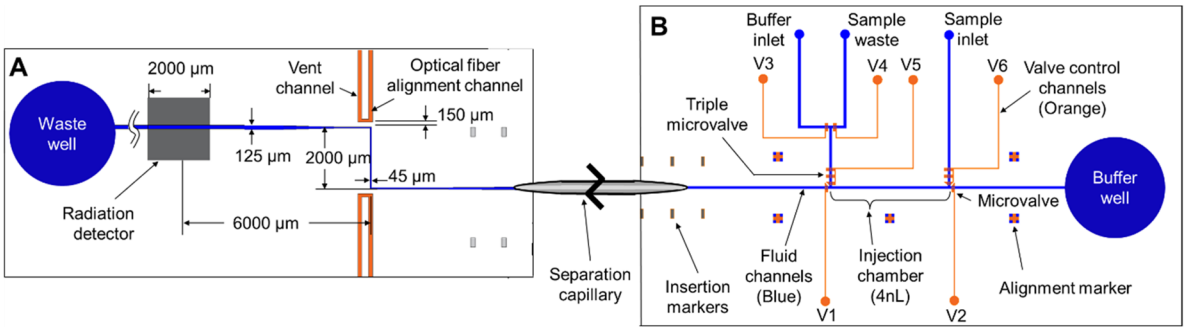

Figure 2. Design of PDMS chips. (A) Detection chip for UV and radiation detection. The channel width tapers down from 125 μm at the right edge of the chip to 45 μm in the optical path to reduce the UV flow cell detection volume. The radiation detector is ∼6 mm downstream of the UV detection region and ∼10 mm upstream of the waste well center. (B) Sample injection chip. Valve control channels (filled with Krytox oil) hydraulically actuate microvalves to control the loading of the 4 nL injection chamber and injection into the capillary for separation. The two chips are connected via the 20 cm long separation capillary. Note that panels A and B are not shown at the same scale.

detect positrons without a scintillator, as shown by Taggart[43] and Salvador,[44] though the efficiency was quite low due to a relatively large source-to-detector distance. One disadvantage of SiPMs is the difficulty in eliminating thermal noise that becomes problematic at low radioactivity levels. To address this, Dooraghi et al. used a 14 mm × 14 mm position-sensitive avalanche photodiode (PSAPD) to measure small amounts of ^{18}F-labeled compounds taken up into biological cells cultured in chambers in an adjacent PDMS microfluidic chip.[39] The APD had very low and easily eliminated noise, fast response, and very high detection efficiency (up to 43% of the maximum 50% achievable for a planar detector on one side of the radioactive source).

Based on the high efficiency and low noise of the APD approach, we present here the first, to our knowledge, hybrid-MCE system with an integrated radiation detector. We characterize this system and, using a device with both UV absorbance and radiation detectors, demonstrate the ability to simultaneously perform chemical purity analysis and radiochemical identity analysis using the PET tracer [^{18}F]3′-deoxy-3′-fluorothymidine [^{18}F]FLT as a model compound. We believe our hybrid-MCE device has potential for use in rapid analysis of radioactive materials, including PET tracers and other radiopharmaceuticals.

MATERIALS AND METHODS

Reagents. Sodium phosphate monobasic (NaH_2PO_4, ≥98%), sodium phosphate dibasic dihydrate (Na_2HPO_4, ≥99.0%), sodium dodecyl sulfate (SDS, ≥98.5%), potassium phosphate monobasic (KH_2PO_4, ≥99.0%), thymidine (≥99%), 2′,3′-didehydro-3′-deoxythymidine (stavudine, ≥98%), and nosyl chloride (97%) were purchased from Sigma−Aldrich (Milwaukee, WI, USA). Zidovudine impurity B (chlorothymidine, CLT, European Pharmacopoeia reference standard) was purchased from LGC Standards (Wesel, Germany). 30 mM phosphate buffer (PB) was prepared via titration of 100 mM solutions of NaH_2PO_4 and Na_2HPO_4 and monitored with a calibrated pH meter (FiveEasy, Mettler Toledo, Columbus, OH, USA). SDS (100 mM) in 30 mM phosphate buffer was prepared by dissolving SDS in 30 mM PB. Separation buffers were prepared with, and reference standards were dissolved in, 18 MΩ-cm deionized (DI) water obtained from a Milli-Q Integral Water Purification system (EMD Millipore, Billerica, MA, USA). All chemicals were of analytical grade and were used as received.

Hybrid-MCE Device. The hybrid-MCE device (Figure 1) comprised a poly(dimethylsiloxane) (PDMS) sample injection chip (to load a precise sample volume), a 20 cm long 75 μm ID fused-silica capillary for separation, and a PDMS detection chip (to perform UV absorbance and radiation detection). The two PDMS chips have been slightly modified from previous designs[33,45] to improve performance and to incorporate the radiation detector.

Injection Chip. The injection chip was fabricated as reported previously[33] but with several modifications as shown in Figure 2B. First, the number of inlets/outlets was reduced to reduce the fluidic connections to the main separation channel. Second, on these connections, we implemented triple microvalves instead of single microvalves to improve electrical isolation from the separation voltage (Supporting Information, Section 1.1).

Operation of the chip was carried out as described previously.[34] Briefly, to load a sample with the new chip design, valves 1, 2, and 3 are closed, while valves 4, 5, and 6 are opened. The sample vial is pressurized to 3 psi, allowing the sample to flow from the inlet, through the injection chamber to the sample waste. Loading is continued until radioactive liquid emerges at the sample waste port. Once the injection chamber is filled, valves 4 and 5 are closed to pressurize the sample and eliminate any microscopic gas bubbles. Finally, sample pressure is removed, and all remaining valves are closed. To inject the sample, valves 1 and 2 are opened, and, after a 0.5 s delay, high voltage is applied between the buffer well of the injection chip and waste well of the detection chip (Figures 2 and 3).

Detection Chip. The previous design of the PDMS detection chip[34] was modified to improve the performance in several ways. The optical path length of the Z-shaped UV absorbance detection cell was extended from 0.5 to 2.0 mm to improve limit of detection (LOD). The height of channels was 125 μm to enable inclusion of channels to align and hold optical fibers (125 μm outer diameter; ThorLabs, Newton, NJ, USA) in line with the optical path of the cell. The optical fibers were connected to the light source (DH-2000-BAL, Ocean Optics, Dunedun, FL, USA) and spectrophotometer (USB-4000, Ocean Optics) as previously described.[34] In the previous version of the detection chip, the width of all channels was also 125 μm. However, to improve separation resolution, we explored a design with decreased volume of the UV absorbance cell, achieved by shrinking the channel width within the optical path from 125 to 45 μm while maintaining the same channel

https://dx.doi.org/10.1021/acs.analchem.9b04827
Anal. Chem. 2020, 92, 3483−3491

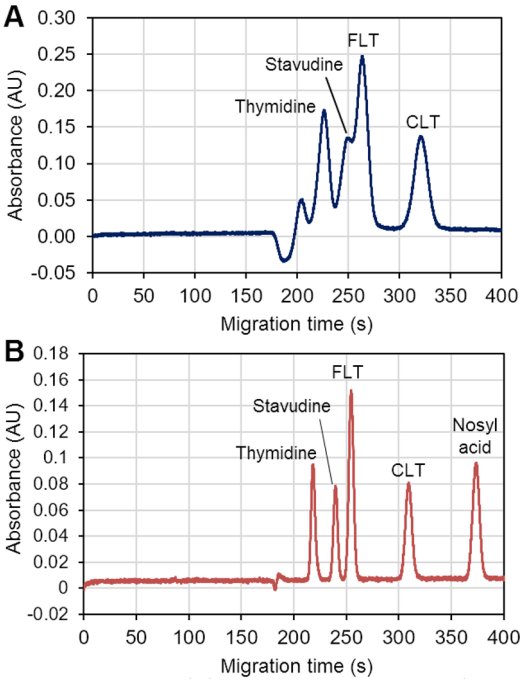

Figure 3. Separation and detection of mixtures of nonradioactive compounds. (A) Electropherogram of a 4-compound mixture (100 μM FLT, 100 μM thymidine, 100 μM stavudine, and 95 μM CLT in DI water) using the detection chip with 125 μm wide optical flow cell. (B) Electropherogram of a 5-compound mixture (250 μM FLT, 250 μM thymidine, 250 μM stavudine, 238 μM CLT, and 250 μM nosyl acid in DI water) using a 45 μm wide optical flow cell.

height (see Figure 2B and Supporting Information, Section 1.2). The UV signal was collected as previously described.[34]

In addition, a radiation detector was integrated into the detection chip. Downstream of the UV absorbance cell, the detection channel crosses over a region with a thin PDMS membrane (100 μm) under which the 2 mm × 2 mm radiation detector is mounted, before terminating in the waste well. Fabrication of the detection chip was described previously,[34] except that the thick bottom PDMS "substrate" was modified to contain a 4 mm × 4 mm square cavity, where the thickness of PDMS was only 100 μm, that was aligned with the radiation detection region (Figure 1B).

Finally, to further improve separation resolution, the capillary-to-chip junction dead volume was reduced by implementing a collinear junction[33,46,47] as also used in the injection chip, by tapering the capillary and inserting it into of the detection channel via the side end of the chip. To stabilize these collinear junctions, channels were filled with DI water, and then degassed liquid PDMS (10:1 mass ratio A:B, RTV615) was applied around the connection and cured at 80 °C for >1 h.

Radiation Detector. Radiation detection was performed using an APD (S0223, Radiation Monitoring Devices Inc., Watertown, MA, USA) with a 2 mm × 2 mm active area biased at 1750 V using a high-voltage power supply (TC952; Tennelec, Oak Ridge, TN, USA). The APD was mounted on an Ultem pillar structure (Figure 1C) designed such that when the detection chip is placed over it, the active surface of the APD is in contact with the bottom side of the thin PDMS membrane within the 4 mm × 4 mm cavity of the bottom PDMS substrate described above.

A thin opaque coating was deposited on the detector to prevent optical photons from triggering the detector while also minimizing attenuation of positrons. The device was first coated with 2 μm of parylene C (Specialty Coating Systems Inc., Indianapolis, IN, USA) using a parylene deposition machine (PDS 2010, Specialty Coating Systems), followed by 350 nm of gold deposited by sputtering (Desk V, Denton Vacuum, Moorestown, NJ, USA), and finally followed by an additional 2 μm of parylene C. This was the lowest thickness that gave an opaque coating such that the detector response in light and dark conditions (with no radioactivity nearby) were the same. The metal layer also served as a Faraday cage, providing electrical shielding of the detector. To form an electrical contact to the gold coating, a thin nichrome wire was attached to the polyether ether ketone (PEEK) pillar via silver epoxy (MG Chemicals, Burlington, Ontario, Canada) before the gold coating, which was later soldered to the circuit ground.

To readout the APD signal, a preamplifying circuit based on a transimpedance amplifier, as described in Dooraghi et al.,[48] was capacitively coupled (1 μF) to the positive terminal of the detector. The signal was processed via a series of amplifiers and analog filters to perform pulse shaping (~200 ns time constant), and then a comparator was used to exclude low-amplitude thermal and electronic noise pulses but retain higher-amplitude pulses from positron interactions (Supporting Information, Section 2). Pulses from the output of the comparator were counted by a data acquisition (DAQ) module (USB-6501, National Instruments, Austin TX, USA). A program written in LabVIEW (National Instruments) recorded the number of counts every 0.5 s (and then reset the counter), and the recorded value was used to determine the count rate per second (cps).

Characterization of Radiation Detector. To investigate the linear range, a detection chip was filled with known concentrations of aqueous [^{18}F]fluoride (11−1600 MBq/mL [0.3−42 mCi/mL]), and the resulting APD signal was measured for each sample. All measurements were performed with a single hybrid-MCE device on a single day. Between each sample, the hybrid-MCE device was cleaned with DI water (1.0 mL) and dried with nitrogen. Due to the possibility of residual radioactivity within or near the channel, a measurement of background was performed prior to each experiment. The average count rate of each 5 min data set (after background subtraction) was plotted versus radioactivity concentration, and a linear fit was calculated. The limit of detection (LOD) and limit of quantitation (LOQ) were calculated from this linear fit as the radioactivity concentrations that would give signals equal to the average background plus 3× and 10× the standard deviation of the background count rate, respectively.

To measure background, the chip was filled with DI water, all radioactive sources were moved away from the detector, and then radiation detector background was measured for 5 min. The average was subtracted from the subsequent data set.

To estimate the size of the detection volume of the detector, Monte Carlo simulations were performed. By exploring the expected detector count rate as a function of the geometry of a microchannel filled with homogeneous radioactivity concentration (Supporting Information, Section 3), we determined that the detector is sensitive to radioactivity up to ~1 mm (in the lateral direction) from the edge of the detector. Thus, for a channel of 125 μm width and 125 μm height crossing the

https://dx.doi.org/10.1021/acs.analchem.9b04827
Anal. Chem. 2020, 92, 3483−3491

radiation detector, >95% of the counts originated from a 4 mm long segment of the channel centered on the detector.

Performing Microchip Electrophoresis. The detection and separation of samples were performed on the hybrid-MCE chip via micellar electrokinetic chromatography (MEKC) as described previously.[33,34] The buffer consists of 30 mM sodium phosphate buffer and 100 mM SDS in DI water. After loading a sample into the injection chamber (~4 nL) of the PDMS injection chip, the sample is separated (in the capillary) by applying ~4 kV between the buffer well in the injection chip and the waste well of the detection chip (field strength 200 V/cm). For all radioactivity measurements, the bias voltage of the APD was turned on for 1 h before injection to allow device to warm up and stabilize.

To demonstrate the utility for assessment of chemical purity, samples of purified PET tracer ([^{18}F]FLT; Supporting Information, Sections 4.1, 4.2) with known concentrations of side-products were injected. Radiochemical identity testing was performed by coinjection of purified [^{18}F]FLT mixed with FLT reference standard. The same samples were also injected into analytical HPLC to confirm radiochemical identity (Supporting Information, Section 4.3).

To estimate the sensitivity to radioactivity of the overall system, hybrid-MCE runs were performed with samples with different radioactivity concentrations of [^{18}F]FLT (2.1−1800 MBq/mL [0.056−49 mCi/mL]). Background was measured for 5 min just prior to each injection and subtracted from the corresponding electropherogram before analysis. All samples were run on the same hybrid-MCE device, on the same day, and were prepared from the same initial batch of [^{18}F]FLT.

Data Analysis. UV Absorbance Signal. Each UV electropherogram was analyzed as described previously[33,34] to determine peak migration time (t_m, taken at peak center), peak width (W_{fwhm}; full width at half-maximum), number of theoretical plates (N), theoretical plate height (H), and peak area (Gaussian fit). For electropherograms with multiple peaks, these parameters were computed for all peaks, and separation resolution was also computed. Briefly, for each peak in the resulting electropherogram, the number of theoretical plates, N, was calculated as $N = 5.54(t_m/W_{fwhm})^2$. The plate height, H, was calculated as $H = L/N$, where L is the effective separation length (21 cm). For mixture samples, the peak resolution, R, between pairs of peaks was computed as $R = 1.18(t_{m2} - t_{m1})/(W_{fwhm,1} + W_{fwhm,2})$, where t_{m1} and t_{m2} are the migration times of the two peaks and $W_{fwhm,1}$ and $W_{fwhm,2}$ are the peak widths. Because the migration time can vary from run to run (e.g., alteration of surface condition or liquid temperature) and migration speed affects the apparent peak area, a time-correction is needed for quantitative peak analysis.

Before further analysis, the time axes were scaled such that the FLT peaks had identical migration time. Following the procedure of Bidulock et al.,[49] where the flow rate during each separation is assumed to be constant, each data set's time-axis is multiplied by the factor t_i/t_0 where t_0 is the measured migration time of FLT for that data set, and t_i is the reference time.

Peaks in mixtures were identified based on migration times determined by injecting individual reference standards.

Radiation Detector Signal. After subtracting the average background, radioelectropherograms were analyzed in a similar manner to UV, including scaling the time-axis to align the [^{18}F]FLT radiation peak migration times to that of the UV peak migration time as described in the Supporting Information, Section 4.3.

Coinjection with FLT reference standard was performed to confirm peak identity and compared with radio HPLC.

Limit of detection was estimated by dividing the standard deviation of the intercept (of the peak area vs radioactivity concentration linear fit) by the slope, to give a critical limit of radioactivity concentration.[50] The LOD and LOQ were defined as 3× and 10× this concentration, respectively. Uncertainties were calculated via standard error propagation formulas.

RESULTS

Separation Efficiency. To assess the separation performance of the overall setup, nonradioactive samples were injected into the hybrid-MCE device with 20 cm capillary length and monitored with the UV absorbance detector. When a mixture of 4 compounds was injected in the device with 125 μm wide optical flow cell, several peaks were overlapping, and baseline separation was not achieved (Figure 3A). However, when we performed the separation of a similar mixture with 5 compounds in the device with 45 μm wide optical flow cell (same optical path length but reduced flow cell volume), baseline separation was achieved for all species (Figure 3B). A detailed comparison of peak parameters is included in Supporting Information Table S3. Notably, with the improved flow cell design, the resolution between the FLT peak and the closest impurity (stavudine) improved from 0.68 (n = 1) to 1.85 ± 0.17 (n = 3), and the number of theoretical plates (for FLT) was increased from 2470 to 11000.

Sensitivity of the device (LOD for FLT of 5 μM) was found to be similar to that of our previous report (3 μM).[34] It also compares favorably with previously characterized commercial CE (6 μM) and HPLC (2 μM) systems.[34] The longer UV path length in this work (2.0 vs 0.5 mm) helped to compensate for the use of a higher-noise spectrometer than we used previously.

Characterization of Radiation Detector. We then studied the performance of the integrated radiation detector. Figure 4 shows the measured average signal as a function of radioactivity concentration when we manually loaded samples to completely fill the detection chip. The resulting data show good linearity (R^2 = 0.994). Combing with the background measurement (0.01 ± 0.12 cps, n = 600), the radioactivity

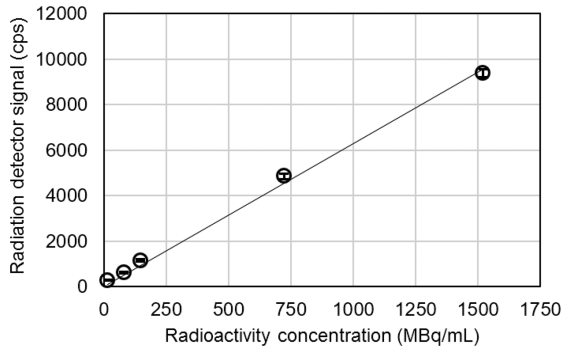

Figure 4. Radiation detector signal when detection channel is uniformly filled with aqueous [^{18}F]fluoride solution of different concentrations. The background has been subtracted from all values. Error bars represent the standard deviation of the 600 detector readings over the 5 min acquisition for each sample. The line is a linear least-squares fit ($y = 6.29x + 0.04$; R^2 = 0.998).

https://dx.doi.org/10.1021/acs.analchem.9b04827
Anal. Chem. 2020, 92, 3483−3491

concentrations corresponding to the LOD and LOQ were estimated to be 590 kBq/mL [16 μCi/mL] and 2.0 MBq/mL [54 μCi/mL], respectively. While these values are well below the typical PET tracer concentrations discussed in the Introduction (i.e., 10 MBq/mL to 10 GBq/mL), we must keep in mind that, based on Monte Carlo simulations, the detector is sensitive to a volume of ~63 nL (4 mm long channel segment, 125 μm wide, 125 μm deep), while the sample injector chip provides a volume of only ~4 nL for each sample; therefore, we expect a deterioration in LOD from this reduction in volume.

Thus, we next used the whole hybrid-MCE setup and performed sample injections of different radioactivity concentrations of [^{18}F]FLT. The resulting electropherograms were analyzed to determine peak area, peak width, and number of theoretical plates (Supporting Information Table S2), and the peak areas were plotted as a function of radioactivity concentration (Figure 5). The peaks were sharp, but

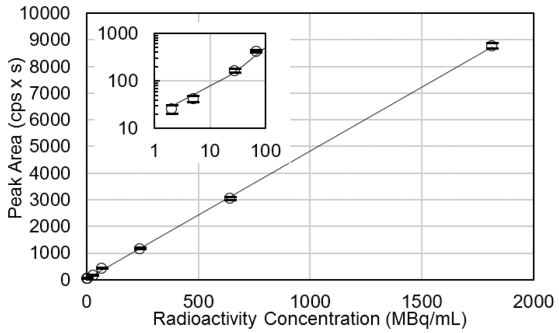

Figure 5. Radioelectropherogram peak area (total counts) as a function of radioactivity concentration of injected samples of purified [^{18}F]FLT. Peaks were time-corrected to the same migration time (140 s). The solid line shows a linear least-squares fit ($y = 4.8x + 19.8$; $R^2 = 0.9998$). Inset shows lowest-concentration points on a log–log plot, with the solid line showing the same fit.

quantitative analysis showed them to be slightly wider than the UV peaks (i.e., 15 s versus 8 s). Analyses also showed that the separation efficiency (N = 3000–15000) was slightly worse than obtained from the UV detector with the 45 μm wide optical flow path (N = 6000–22000). The LOD and LOQ were estimated to be 34 MBq/mL (0.9 mCi/mL) and 114 MBq/mL (3.1 mCi/mL), respectively. A summary of figures of merit for samples injected to explore the radiation detector LOD is shown in Supporting Information Table S2.

Demonstration of Radio-MCE Separation. First, a sample of purified and formulated [18F]FLT was analyzed with the hybrid-MCE device. With a concentration of 700 MBq/mL (19 mCi/mL), the total injected radioactivity in the 4 nL sample plug was ~2.8 kBq (~76 nCi). A large peak was observed in the radioactivity electropherogram (Figure 6A), and a corresponding small peak was observed in the UV electropherogram. There were no UV impurity peaks observed at the expected times of known impurities, though a small, unknown radioactive impurity peak was observed at 240 s (~3.5% of the area of all peaks in the radiation detector electropherogram), which was not seen in the corresponding radio HPLC chromatogram (Supporting Information Figure S9). This may suggest some remaining sample from a previous run, or a species whose migration time in CE is different than its HPLC retention time. To verify radiochemical identity, the

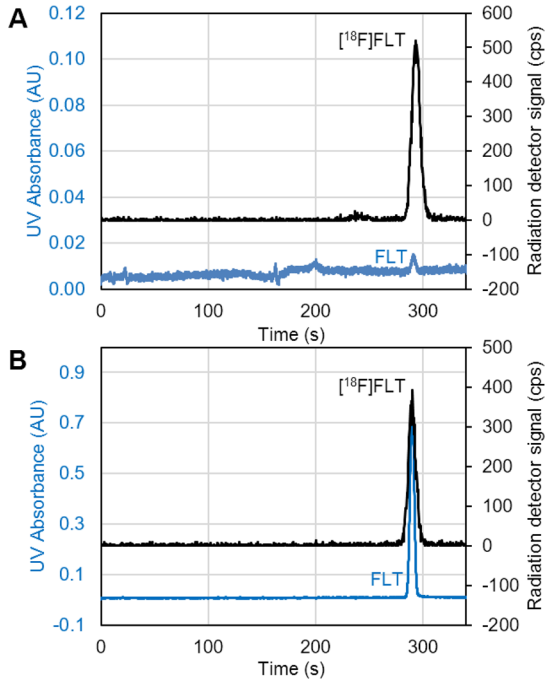

Figure 6. Example dual-modality electropherogram from a sample of (A) purified/formulated [^{18}F]FLT and (B) the same sample coinjected with 500 μM FLT (reference standard). UV absorbance signal is shown in blue, and the radiation detector signal is shown in black.

same [18F]FLT sample was spiked with the FLT reference standard giving a solution with ~500 μM FLT and a radioactivity concentration of 630 MBq/mL (17 mCi/mL). A single peak was observed in the radioelectropherogram Figure 6B, and a single large peak was observed in the UV electropherogram. A summary of the analysis is given in Supporting Information Table S4. Analytical HPLC analysis of the same sample showed a single UV and radiation peak at a retention time of 5.5 min, with the coinjection confirming the identity of FLT.

A sample of crude [^{18}F]FLT (before purification) was also analyzed (Figure 7 and Supporting Information Table S5). From the UV electropherogram, the major side products stavudine, thymidine, and CLT were observed, as well as another significant peak. This impurity has been observed by

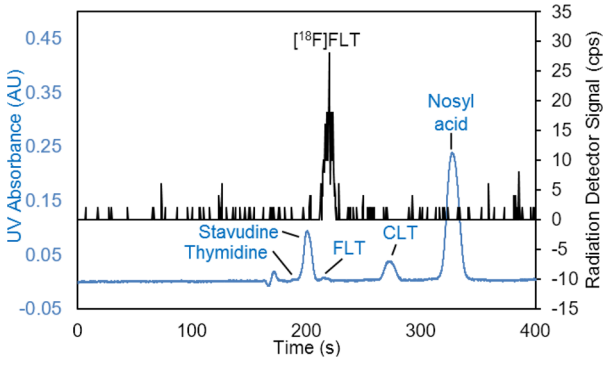

Figure 7. Superimposed electropherograms of crude [^{18}F]FLT product (nonpurified sample). Radioactivity concentration is ~30 MBq/mL. For this sample, a detection chip with a 125 μm wide optical cell was used.

https://dx.doi.org/10.1021/acs.analchem.9b04827
Anal. Chem. 2020, 92, 3483–3491

other investigators but not identified.[51] Here we observe that the impurity appears to coincide with the migration time of nosyl acid, the byproduct resulting from removal of the leaving group when the precursor is fluorinated. During purification, we collected the fraction corresponding to this peak and also confirmed its identity via analytical HPLC. The retention time matched that of nosyl chloride dissolved in DI water, and a coinjection of the collected fraction with nosyl acid exhibited only a single, larger UV peak.

DISCUSSION

The modified UV detection cell (45 μm wide channel instead of 125 μm) significantly improved the separation efficiency and resolution (Figure 4). However, the peak heights were lower after accounting for concentration differences; we suspect the lower signal is due to the channel width (45 μm) being smaller than the diameter of the optical fiber (100 μm ID); such a situation could allow some illumination light to directly reach the detector without interacting with the sample or cause a reduced amount of light to reach the detector. Improvements in optical coupling (e.g., focusing UV into a narrower beam), or further increase of optical path length, could improve the LOD. The detection chip was capable of simultaneously monitoring the UV absorbance and radiation signals. Due to the difference in positioning, there is a time delay between UV and radiation detectors that requires correction by scaling the time axis to align and coregister radiation peaks with UV. For ~4 nL injected samples, the radiation detector had LOD and LOQ of 34 MBq/mL (0.9 mCi/mL) and 114 MBq/mL (3.1 mCi/mL), respectively, for ^{18}F-labeled compounds. (Interestingly, if we use the maximum theoretical molar activity of F-18 to estimate the number of radioactive molecules, these values correspond to 0.54 and 1.8 nM, respectively, which is significantly more sensitive than the UV detector.) The typical radioactivity concentration of a formulated PET tracer is in the range 37−11000 MBq/mL (1−300 mCi/mL), depending on whether a single patient dose is prepared or a large multipatient batch. Compared to the sensitivity, it would be possible to detect low-abundance impurities (for purposes of quantifying radiochemical purity, as low as 0.5% of the major peak[36]) in samples with radioactivity concentrations toward the higher end of this range. However, for smaller batches improvement in sensitivity is needed and is the focus of ongoing studies. One route to improve the LOQ would be to increase the radiation signal by (i) increasing the total injected radioactivity, such as increasing the sample injection volume (currently only 4 nL compared to 10 s of μL used in analytical radio-HPLC), (ii) performing online preconcentration of the sample, or (iii) modifying the detection cell to increase the residence time. Another way to improve the LOQ would be to reduce the level of noise in the system. For example, results from Dooraghi et al.[39] suggest that for our 4 mm^2 detector area that the background in an APD detector could be as low as ~3.2 counts/h (8×10^{-4} cps) resulting from cosmic rays. In comparison, we observed background noise of ~0.04 ± 0.12 cps, indicating room for improvement through optimization of the radiation detector geometry and electronics.

The use of an APD for radiation detector has a number of advantages compared to scintillator-PMT approaches but also introduces a few challenges. The sensitivity only to short-range particles enables high resolution (localized detection) without the need for bulky radiation shielding but requires close positioning to the sample. Electrical shielding was critical to avoid interference from the separation channel but could be achieved with a thin coating of an insulation layer and conductive metal layer (which also shielded against ambient light). While the APD would have limited sensitivity and resolution when working with gamma-emitting species, it is suitable for beta-emitting radioactive species, which includes any PET radiopharmaceuticals as well as many SPECT and theranostic radiopharmaceuticals.

CONCLUSIONS

A novel hybrid-MCE device was developed to analyze radioactive compounds following electrophoretic separation. In a set of preliminary demonstrations, the radiolabeled PET tracer [^{18}F]FLT was successfully detected by both the positron detector and an integrated UV absorbance detector and was separated from impurities present in the sample. The system can perform chemical and radiochemical identity tests and can perform chemical and radiochemical purity tests.

Using the UV detector, the LOQ of FLT was 17 μM, and using the radiation detector, the LOQ of [^{18}F]FLT was 114 MBq/mL (3.1 mCi/mL) for a 4 nL sample injection volume. While adequate for many analysis applications, including analysis of radiochemical purity of radiopharmaceuticals with high radioactivity concentration (e.g., large multipatient batches prepared in radiopharmacies for distribution to imaging sites), improvements in sensitivity would expand the use of this setup to smaller, more dilute batches, e.g., for research purposes or for batches intended for smaller numbers of patient. Studies are ongoing to improve the detection sensitivity for both UV and radiation detectors. Wider adoption would also require further development and refinement and simplification of the hybrid-MCE device and its operation and would likely require the development of separation methods for additional radiopharmaceuticals and comparisons to radio-HPLC.

In addition to chemical and radiochemical analysis of samples, we are also exploring whether additional quality control tests, such as molar activity and half-life, can be performed in the system.

We expect the radiation detector is not limited to analysis of ^{18}F-labeled compounds but would also be suitable for the detection of other positron-emitting isotopes, as well as beta-emitting isotopes (e.g., Lu-177), and potentially alpha-emitting isotopes (e.g., Ac-225) used in radiopharmaceuticals for targeted radionuclide therapy.

ASSOCIATED CONTENT

Supporting Information

The Supporting Information is available free of charge at https://pubs.acs.org/doi/10.1021/acs.analchem.9b04827.

Hybrid-MCE chip fabrication, radiation detector circuitry, Monte Carlo simulations, synthesis of [^{18}F]FLT, limit of detection analysis, hybrid-MCE control system, and radioelectropherogram figures of merit (PDF)

AUTHOR INFORMATION

Corresponding Author

R. Michael van Dam − *Crump Institute for Molecular Imaging and Department of Molecular and Medical Pharmacology, David Geffen School of Medicine, Physics & Biology in Medicine Interdepartmental Graduate Program, David Geffen School of Medicine, Department of Bioengineering, Henry Samueli School*

https://dx.doi.org/10.1021/acs.analchem.9b04827
Anal. Chem. 2020, 92, 3483−3491

of Engineering and Applied Science, and Department of Molecular & Medical Pharmacology, University of California Los Angeles, Los Angeles, California 90095, United States; Email: mvandam@mednet.ucla.edu

Authors

Jason Jones − *Crump Institute for Molecular Imaging and Department of Molecular and Medical Pharmacology, David Geffen School of Medicine and Physics & Biology in Medicine Interdepartmental Graduate Program, David Geffen School of Medicine, University of California Los Angeles, Los Angeles, California 90095, United States*; orcid.org/0000-0003-0140-1087

Noel S. Ha − *Crump Institute for Molecular Imaging and Department of Molecular and Medical Pharmacology, David Geffen School of Medicine and Department of Bioengineering, Henry Samueli School of Engineering and Applied Science, University of California Los Angeles, Los Angeles, California 90095, United States*; orcid.org/0000-0002-3275-577X

Alec G. Barajas − *Crump Institute for Molecular Imaging and Department of Molecular and Medical Pharmacology, David Geffen School of Medicine and Department of Chemistry & Biochemistry, University of California Los Angeles, Los Angeles, California 90095, United States*

Arion F. Chatziioannou − *Crump Institute for Molecular Imaging and Department of Molecular and Medical Pharmacology, David Geffen School of Medicine, Physics & Biology in Medicine Interdepartmental Graduate Program, David Geffen School of Medicine, and Department of Molecular & Medical Pharmacology, University of California Los Angeles, Los Angeles, California 90095, United States*

Complete contact information is available at: https://pubs.acs.org/10.1021/acs.analchem.9b04827

Author Contributions

J.J. and N.S.H. contributed equally to this work.

Notes

The authors declare no competing financial interest.

■ ACKNOWLEDGMENTS

This work was supported in part by the National Institute on Aging (R21 AG049918), the National Cancer Institute (R21 CA212718), the National Institute of Biomedical Imaging and Bioengineering (R21 EB024243, T32 EB002101), and the UCLA Foundation from a donation made by Ralph & Marjorie Crump for the UCLA Crump Institute for Molecular Imaging. The authors thank Dr. Roger Slavik and the staff of the UCLA Biomedical Cyclotron Facility for generously providing [^{18}F] fluoride for these studies. The authors also thank Dr. David Prout for the help with the radiation detection setup, Dr. Jason T. Lee for providing the space for the experimental setup at the Crump Preclinical Imaging Technology Center, R. W. Silverman for assistance with radiation detector electronics and helpful discussions, and Dr. Patrice Marchand for helpful discussions about identification of the impurity in [^{18}F]FLT synthesis. The authors also acknowledge the use of the Integrated Systems Nanofabrication Cleanroom at the California NanoSystems Institute.

■ REFERENCES

(1) Mironov, G. G.; Clouthier, C. M.; Akbar, A.; Keillor, J. W.; Berezovski, M. V. *Nat. Chem. Biol.* **2016**, *12*, 918.
(2) Morbioli, G. G.; Mazzu-Nascimento, T.; Aquino, A.; Cervantes, C.; Carrilho, E. *Anal. Chim. Acta* **2016**, *935*, 44−57.
(3) Durney, B. C.; Crihfield, C. L.; Holland, L. A. *Anal. Bioanal. Chem.* **2015**, *407* (23), 6923−6938.
(4) Ruokonen, S.-K.; Duša, F.; Lokajová, J.; Kilpeläinen, I.; King, A. W. T.; Wiedmer, S. K. *J. Chromatogr. A* **2015**, *1405*, 178−187.
(5) Skelley, A. M.; Scherer, J. R.; Aubrey, A. D.; Grover, W. H.; Ivester, R. H. C.; Ehrenfreund, P.; Grunthaner, F. J.; Bada, J. L.; Mathies, R. A. *Proc. Natl. Acad. Sci. U. S. A.* **2005**, *102* (4), 1041−1046.
(6) Lian, D.-S.; Zeng, H.-S. *Compr. Rev. Food Sci. Food Saf.* **2017**, *16* (6), 1281−1295.
(7) Gomez, F. J. V.; Silva, M. F. *Anal. Bioanal. Chem.* **2016**, *408*, 8643−8653.
(8) Calcerrada, M.; González-Herráez, M.; García-Ruiz, C. *TrAC Trends Anal. Chem.* **2016**, *75*, 75−85.
(9) Altria, K. D. *J. Chromatogr. A* **1999**, *856* (1−2), 443−463.
(10) Bowen, A. L.; Martin, R. S. *Electrophoresis* **2010**, *31* (15), 2534−2540.
(11) Kubáň, P.; Hauser, P. C. *Lab Chip* **2005**, *5* (4), 407−415.
(12) Kubáň, P.; Hauser, P. C. *Anal. Chim. Acta* **2008**, *607* (1), 15−29.
(13) Kubáň, P.; Hauser, P. C. *Electrophoresis* **2009**, *30* (1), 176−188.
(14) Bruno, A. E.; Krattiger, B.; Maystre, F.; Widmer, H. M. *Anal. Chem.* **1991**, *63* (23), 2689−2697.
(15) Redman, E. A.; Mellors, J. S.; Starkey, J. A.; Ramsey, J. M. *Anal. Chem.* **2016**, *88* (4), 2220−2226.
(16) Chen, X.; Tang, K.; Lee, M.; Flynn, G. C. *Electrophoresis* **2008**, *29* (24), 4993−5002.
(17) Ruiz-Martinez, M. C.; Berka, J.; Belenkii, A.; Foret, F.; Miller, A. W.; Karger, B. L. *Anal. Chem.* **1993**, *65* (20), 2851−2858.
(18) Dovichi, N. J.; Zhang, J. *Angew. Chem., Int. Ed.* **2000**, *39* (24), 4463−4468.
(19) Pentoney, S. L.; Zare, R. N.; Quint, J. F. *Anal. Chem.* **1989**, *61* (15), 1642−1647.
(20) Jankowsky, R.; Noll, B.; Johannsen, B. *J. Chromatogr., Biomed. Appl.* **1999**, *724* (2), 365−371.
(21) Pitois, A.; Aldave de Las Heras, L.; Betti, M. *Int. J. Mass Spectrom.* **2008**, *270* (3), 118−126.
(22) Martelat, B.; Isnard, H.; Vio, L.; Dupuis, E.; Cornet, T.; Nonell, A.; Chartier, F. *Anal. Chem.* **2018**, *90* (14), 8622−8628.
(23) Altria, K. D.; Simpson, C. F.; Bharij, A. K.; Theobald, A. E. *Electrophoresis* **1990**, *11* (9), 732−734.
(24) Jankowsky, R.; Friebe, M.; Noll, B.; Johannsen, B. *J. Chromatogr. A* **1999**, *833* (1), 83−96.
(25) Klunder, G. L.; Andrews, J. E.; Grant, P. M.; Andresen, B. D.; Russo, R. E. *Anal. Chem.* **1997**, *69* (15), 2988−2993.
(26) Kaniansky, D.; Rajec, P.; Švec, A.; Marák, J.; Kovaľ, M.; Lúčka, M.; Franko, Š.; Sabanoš, G. *J. Radioanal. Nucl. Chem.* **1989**, *129* (2), 305−325.
(27) Pentoney, S. L.; Zare, R. N.; Quint, J. F. *J. Chromatogr. A* **1989**, *480*, 259−270.
(28) Cheung, S.; Ly, J.; Lazari, M.; Sadeghi, S.; Keng, P. Y.; van Dam, R. M. *J. Pharm. Biomed. Anal.* **2014**, *94*, 12−18.
(29) Castro, E. R.; Manz, A. *J. Chromatogr. A* **2015**, *1382*, 66−85.
(30) Dawod, M.; Arvin, N. E.; Kennedy, R. T. *Analyst* **2017**, *142* (11), 1847−1866.
(31) Ha, N. S.; Sadeghi, S.; van Dam, R. M. *Micromachines* **2017**, *8* (11), 337.
(32) Pascali, G.; Watts, P.; Salvadori, P. *Nucl. Med. Biol.* **2013**, *40* (6), 776−787.
(33) Ha, N. S.; Ly, J.; Jones, J.; Cheung, S.; van Dam, R. M. *Anal. Chim. Acta* **2017**, *985*, 129−140.
(34) Ly, J.; Ha, N. S.; Cheung, S.; van Dam, R. M. *Anal. Bioanal. Chem.* **2018**, *410* (9), 2423−2436.
(35) Fermi, E. Quality Control of PET Radiopharmaceuticals. In *Molecular Imaging: Radiopharmaceuticals for PET and SPECT*; Springer: Berlin Heidelberg, 2009; pp 197−204, DOI: 10.1007/978-3-540-76735-0_13.

(36) U.S. Pharmacopeia (USP). *General Chapter <823>: Positron Emission Tomography Drugs for Compounding, Investigation, and Research Uses*; USP: Rockville, MD, USA, November 2011.
(37) European Pharmacopeia (EP). *Technical Guide for the Elaboration of Monographs on Radiopharmaceutical Preparations*; European Directorate for the Quality of Medicines & Healthcare: Strasbourg, France, 2010.
(38) Thonon, D.; Kaisin, G.; Henrottin, J.; Aerts, J.; Van Malderen, H.; Luxen, A. *Appl. Radiat. Isot.* **2013**, *73*, 84−89.
(39) Dooraghi, A. A.; Vu, N. T.; Silverman, R. W.; Farrell, R.; Shah, K. S.; Wang, J.; Heath, J. R.; Chatziioannou, A. F. *Phys. Med. Biol.* **2013**, *58* (11), 3739.
(40) Sanchez-Crespo, A. *Appl. Radiat. Isot.* **2013**, *76*, 55−62.
(41) Cho, J. S.; Vu, N. T.; Chung, Y. H.; Yu, Z. T.; Silverman, R. W.; Taschereau, R.; Tseng, H. R.; Chatziioannou, A. F. Detection of Beta Particles in a Microfluidic Chip Using a Scintillator and CCD. In *2006 IEEE Nuclear Science Symposium Conference Record*; 2006; Vol. *4*, pp 1977−1981, DOI: 10.1109/NSSMIC.2006.354301.
(42) Tarn, M. D.; Kızılyer, N. Y.; Esfahani, M. M. N.; Joshi, P.; Brown, N. J.; Pamme, N.; Jenkins, D. G.; Archibald, S. J. *Chem. - Eur. J.* **2018**, *24* (52), 13749−13753.
(43) Taggart, M. P.; Tarn, M. D.; Esfahani, M. M. N.; Schofield, D. M.; Brown, N. J.; Archibald, S. J.; Deakin, T.; Pamme, N.; Thompson, L. F. *Lab Chip* **2016**, *16* (9), 1605−1616.
(44) Salvador, B.; Escalante, D.; Fernandez-Maza, L.; Corral, A.; Camacho-Leon, S.; Luque, A. *IEEE Sens. J.* **2019**, *19* (17), 7702−7707.
(45) Ly, J. Chemical Purity Analysis of PET Radiotracers via Microchip Capillary Electrophoresis. Ph.D., University of California, Los Angeles, 2016.
(46) Bings, N. H.; Wang, C.; Skinner, C. D.; Colyer, C. L.; Thibault, P.; Harrison, D. J. *Anal. Chem.* **1999**, *71* (15), 3292−3296.
(47) Chiou, C.-H.; Lee, G.-B. *J. Micromech. Microeng.* **2004**, *14* (11), 1484.
(48) Dooraghi, A. A.; Silverman, R. W.; Prout, D. L.; Tashereau, R.; Vu, N. T.; Chatziioannou, A. F. Evaluation of Transimpedance Amplifiers for Readout of a Position Sensitive Avalanche Photodiode. In *2011 IEEE Nuclear Science Symposium Conference Record*; 2011; pp 924−927, DOI: 10.1109/NSSMIC.2011.6154572.
(49) Bidulock, A. C. E.; van den Berg, A.; Eijkel, J. C. T. *Electrophoresis* **2015**, *36* (6), 875−883.
(50) Wisconsin Department of Natural Resources Laboratory Certification Program. *Analytical Detection Limit Guidance & Laboratory Guide for Determining Method Detection Limits*. https://dnr.wi.gov/regulations/labcert/documents/guidance/-lodguide.pdf (accessed Aug 13, 2019).
(51) Marchand, P.; Ouadi, A.; Pellicioli, M.; Schuler, J.; Laquerriere, P.; Boisson, F.; Brasse, D. *Nucl. Med. Biol.* **2016**, *43* (8), 520−527.

https://dx.doi.org/10.1021/acs.analchem.9b04827
Anal. Chem. 2020, 92, 3483−3491